Geophysical and Astrophysical Fluid Dynamics
Vol. 00, No. 00, 00 Month 20xx, 1–18

Robustness of the structure of general atmospheric circulation under global cooling

Andrei Sukhanovskii[1*] and Andrei Gavrilov[2]

[1]Institute of Continuous Media Mechanics UB RAS, Academ. Korolyov, Perm, 614013, Russia
[2]Kutateladze Institute of Thermophysics SB RAS, Lavrenteva av. 1, Novosibirsk, 630090, Russia

(*November 2025*)

Numerical simulations using an idealized laboratory-scale model were employed to study the transformation of the general circulation of the atmosphere under conditions of global cooling. The focus was on structural changes in circulation as the temperature gradient decreased. It was found that the structure of the general circulation is very robust and practically does not change with decreased heating. Even with 20% of the initial heating power, the mean circulation consists of three cells: Hadley, Ferrel, and polar. However, the magnitudes of the main characteristics, such as maximum velocity and temperature difference, significantly decrease with reduced heating. Blockings of baroclinic waves appear even with constant zonally symmetric boundary conditions. A noticeable time lag was found between temperature and radial velocity pulsations. Decomposing the baroclinic waves into Fourier modes reveals remarkable similarities in the energy spectra and spatial energy distribution to those obtained in a full-scale, idealized simulation of an Earth-like atmosphere.

Keywords: general atmosphere circulation, global cooling, idealized model, rotating convection

1. Introduction

The general atmospheric circulation plays a crucial role in weather formation and climate change. It consists of three meridional cells, the Hadley cell in the low latitudes, the Ferrel cell in the mid-latitudes and the polar cell in the high latitudes Vallis (2017). The Ferrel cell is generated by the mean action of baroclinic waves, which transfer heat and angular momentum from pole to equator in the mid-latitudes Schneider (2006). Despite its size and the complex set of hydrodynamic and thermodynamic processes, the global circulation can be considered a rotating convection system driven by the temperature difference between the equator and the poles. This concept has motivated a large number of laboratory studies devoted to modeling different aspects of the global circulation, focusing on baroclinic waves Read *et al.* (2014). There are two main alternative laboratory approaches to studying baroclinic waves: the dishpan configuration (Fultz *et al.* 1959), and the annulus configuration (Hide 1953). The Fultz configuration, also known as the dishpan configuration, is a cylindrical vessel that is usually horizontally extended. It has rim heating at the bottom periphery and cooling in the center. The Hide configuration, also known as the annulus configuration, is a cylindrical gap between inner and outer cylinders. It has isothermal vertical walls, with the inner wall being cold and the outer wall being hot. The specifics and comparison of recent results for both configurations are described and discussed in (Harlander *et al.* 2023, 2024). Experiments and numerical simulations (Batalov *et al.* 2010, Sukhanovskii *et al.* 2023, Vasiliev *et al.* 2023) have shown that, within a narrow range of parameters, the large-scale circulation in the Fultz configuration is

*Corresponding author. Email: san@icmm.ru

qualitatively similar to the Earth's circulation, including mid-latitude baroclinic waves. The apparent similarity in flow structure and the main mechanisms responsible for flow formation make idealized laboratory models a useful tool for revealing fundamental properties of large-scale atmospheric flows and their sensitivity to variations in key parameters.

For the fixed aspect ratio there are two main parameters that define the formation of the global circulation in a rotating layer with a meridional temperature gradient: rotation and heating power. The remarkable structural changes with a variation of rotation rate for different configurations were shown in (Sukhanovskii *et al.* 2023, Gavrilov *et al.* 2025, Meletti *et al.* 2025). Relatively small increasing or decreasing in rotation rate leads to the critical changes in the flow structure. This study focuses on the second key parameter: the meridional temperature gradient. There are two main scenarios that may lead to the decrease of the meridional temperature difference. The first is associated with Arcic warming amplification (You *et al.* 2021), which has been studied using laboratory (Vincze *et al.* 2017, Rodda *et al.* 2022, Sukhanovskii *et al.* 2024) and climatic models (Smith *et al.* 2019, Ye *et al.* 2024), as well as reanalysis (Blackport and Screen 2020). Laboratory modeling (Sukhanovskii *et al.* 2024) showed that turning off Arctic cooling does not lead to drastic changes in the mid-latitude circulation and baroclinic wave dynamics, mainly due to the Arctic's relatively small area and total cooling power (compared to the equator). This is consistent with the results of climate modeling (Smith *et al.* 2019, Ye *et al.* 2024) and reanalysis (Blackport and Screen 2020). The second scenario, which may have catastrophic consequences, is connected with a significant reduction in solar radiation (global cooling) due to increased atmospheric aerosol concentration. Supervolcano eruptions and nuclear wars are possible sources of massive aerosol production, leading to volcanic or nuclear winters (Coupe and Robock 2021). Most studies on the impact of volcanic eruptions have focused on mean global characteristics and surface and ocean temperature distributions or regional events Timmreck (2012), Marshall *et al.* (2022), Zuo *et al.* (2022), Zhou and Liu (2024). There is a general consensus that an increase in aerosol concentrations will result in a decrease in the global mean temperature of the troposphere, oceans, and land surfaces. However, the problem of structural changes in the global atmospheric circulation receives much less attention. Most studies focus on stratospheric flows because atmospheric aerosols substantially warm the stratosphere (DallaSanta *et al.* 2019, Tian *et al.* 2023). We believe that idealized modeling will reveal the main aspects of how a decrease in solar heating impacts the large-scale atmospheric circulation. Therefore, the main issue we address in the present study is structural change in a laboratory model of general atmospheric circulation under global cooling.

The structure of the paper is as follows. The methods are described in section 2. The main results, including description of the flow structure changes and properties of baroclinic waves are presented in section 3. A summary and conclusions are given in section 4.

2. Methods

In the present study, we performed a series of numerical simulations using a digital "twin" of the laboratory model of general atmospheric circulation. A detailed description of the laboratory model, as well as a comparison of the laboratory and numerical results, can be found in (Sukhanovskii *et al.* 2023, 2024, Gavrilov *et al.* 2025). The model consists of a rotating layer of fluid with an open, cooled surface and a rim heater at the bottom. The rim heater mimics equatorial heating, and it is intentionally shifted from the sidewall to minimize the effect of non-slip vertical boundaries. The boundary conditions of the second type (constant heat flux) were chosen because they are more realistic for the atmosphere. Within a specific, very narrow range of control parameters (i.e., atmospheric regime), the large-scale circulation resembles that of the general atmosphere (see Fig. 1). The mean meridional circulation in

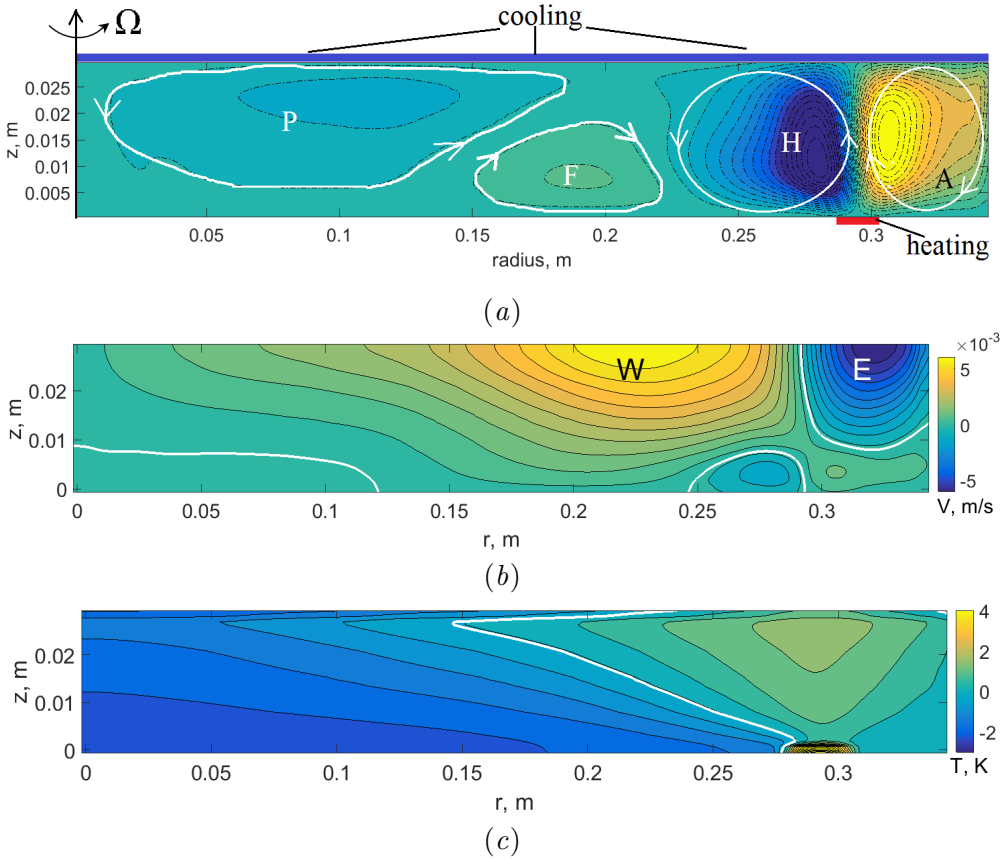

Figure 1. Typical flow structure and temperature field of the laboratory model of general atmosphere circulation (a) mean meridional circulation , P – analog of polar cell, F – analog of Ferrel cell, H – analog of Hadley cell, A – additional sidewall cell,the colored background shows the values of the stream function, (b) mean zonal circulation, W – analog of westerly winds, E – analog of easterly winds, white solid line corresponds to zero values of V, (c) mean temperature distribution, white solid line corresponds to zero values of T. (Colour online)

the atmospheric regime (Fig. 1a) includes analogs of the polar cell at small radii and the weak Ferrel cell at middle radii. The Ferrel cell is only visible after averaging over the zonal coordinate and time. The Hadley cell is located at the periphery. Note that shifting the heater from the sidewall leads to the formation of an additional cell to the right of the Hadley cell analog (marked A). The mean meridional circulation results in differential rotation and zonal flows, which are analogs of westerly and easterly winds (Fig. 1b). The mean temperature field is characterized by inclined isotherms, a feature typical for baroclinic instability (Fig. 1c).

The simulations were performed with a finite volume in-house CFD code, σFlow. The main parameters are similar to those used in the laboratory experiments. The working volume is a cylindrical fluid layer with a free surface of radius $R = 345$ mm and height $h = 30$ mm. The heater is a 25 mm wide circular strip. The distance from the cylindrical sidewall to the outer border of the heater is 40 mm. The silicon oil PMS-5 (density $\rho = 911$ kgm^{-3}, kinematic viscosity $\nu = 5.2 \times 10^{-6}$ m^{2}s^{-1}, thermal diffusivity $\kappa = 8.3 \times 10^{-8}$ m^{2}s^{-1}, thermal expansion coefficient $\alpha = 9 \times 10^{-4}$ K^{-1}, Prandtl number $\mathrm{Pr} = \nu\kappa^{-1} = 62.7$) is used as the working fluid. The unsteady flow of an incompressible fluid is modeled in the Boussinesq approximation in a rotating reference frame. The unsteady equations in a rotating frame of reference are formulated in terms of the relative velocity components:

$$\nabla \cdot \mathbf{u} = 0,$$

$$\frac{\partial \mathbf{u}}{\partial t} + (\mathbf{u} \cdot \nabla)\,\mathbf{u} + (2\boldsymbol{\Omega} \times \mathbf{u} + \boldsymbol{\Omega} \times \boldsymbol{\Omega} \times \mathbf{r}) = -\frac{\nabla p}{\rho} + \nu \nabla^2 \mathbf{u} - \alpha\,(T - T_0)\,g,$$

$$\frac{\partial T}{\partial t} + (\mathbf{u} \cdot \nabla)\,T = \kappa \nabla^2 T,$$

where $\mathbf{u}$ is the relative velocity vector, ρ is the density, T is the temperature, T_0 is the reference temperature, p is the pressure, $\mathbf{g}$ is the gravitational acceleration, $\mathbf{r}$ is the position vector relative to the rotation center, ν is a kinematic viscosity, Ω is the rotation vector, α is the coefficient of thermal expansion, and κ is the coefficient of thermal diffusivity.

Boundary conditions. The boundary conditions are chosen to mimic the experimental apparatus. On all solid walls no-slip conditions are set. On the free boundary a slip condition is imposed. Constant uniform heat flux densities q are set on the heater, cooler and free surface, which are determined by the given thermal power of the corresponding surface:

$$\frac{\partial T}{\partial n} = -\frac{q}{\lambda},$$

where λ is the thermal conductivity. The heat power of the free surface is equal to the difference between the powers of the heater and the cooler. The other surfaces are adiabatic.

As an initial approximation for velocity, the condition of solid-body rotation with a given rotation speed is set. The initial uniform temperature of the fluid is equal to the reference temperature $T_0 = 293.15$ K.

Discretization. The numerical algorithm is based on the finite volume method for the unstructured mesh. The unstructured computational grid is constructed from several blocks with a structured hexagonal mesh. Approximately the basic grid has the following spatial discretization: $N_r = 192$ nodes in radial direction with clustering of nodes to the heater and cooler, $N_\phi = 260$ nodes in tangential direction and $N_z = 40$ nodes in vertical direction with clustering factor to the boundaries 1.05. The total number of control volumes is about 2.0 million cells. The time step remained constant during the calculation and was set to 0.05 s. The maximum Courant number (CFL) calculated using the relative velocity does not exceed unity, and the volume average CFL = 0.085. The mean characteristics are obtained by averaging over time and along a uniform zonal direction after reaching the statistical steady state regime, which takes about 2000 s. The averaging time is at least 7600 s.

Verification of the simulation was performed by comparing numerical results obtained on three different meshes. Verification calculations were performed for the basic mode at the rotation rate $\Omega = 0.23$ rad s^{-1} and the heat power $Q_h = 123$ W. The grid convergence index (GCI), obtained by comparing the results on the detailed and basic grids, does not exceed 5%. A detailed description of the numerical algorithm and verification procedure can be found in (Sukhanovskii *et al.* 2024).

3. Results

The present study focuses on structural changes in the laboratory model of the global atmospheric circulation with a decrease in equatorial heating. To achieve this, we only vary the magnitude of the heat fluxes at the lower and upper boundaries while maintaining heat flux balance. Because the total heat flux in the system is always zero, the mean temperature remains constant across all cases. We considered two configurations: the first with uniform cooling at the top layer and the second with increased cooling at the center, which models Arctic cooling. In both configurations, heating occurred through a constant heat flux in the

Table 1. Values of thermal Rossby number $\mathrm{Ro_T}$ for the regular ($\mathrm{Ta} = 1.4 \times 10^9$) and irregular ($\mathrm{Ta} = 3.6 \times 10^9$) baroclinic wave regimes.

Heating power	100%	80%	60%	40%	20%
$\mathrm{Ta} = 1.4 \times 10^9$	0.6	0.52	0.43	0.33	0.2
$\mathrm{Ta} = 3.6 \times 10^9$	0.25	0.22	0.18	0.14	0.08

rim area at the bottom. The results for both configurations are generally similar, so we describe the results of the first configuration, which has uniform cooling at the top free surface, in detail.

The rotation rate is a key parameter that determines the structure of large-scale circulation and the characteristics of baroclinic waves. A notable feature of the described system is that the transition from axisymmetric Hadley circulation to irregular wave regime occurs within a relatively narrow range of rotation rates (Sukhanovskii *et al.* 2023, Gavrilov *et al.* 2025, Meletti *et al.* 2025). We considered two flow regimes: regular and irregular baroclinic waves. The rotation rates were set to $\Omega = 0.23$ rad/s and $\Omega = 0.37$ rad/s, respectively. The basic heating power was set to $Q_h = 123$ W. The latter regime most closely resembles real atmospheric circulation, and most of the results correspond to this regime. For the two selected regimes, we varied the heating and cooling power from 100% (the basic condition) to 20% in 20% increments.

As non-dimensional governing parameters, we use the Taylor number $\mathrm{Ta} = 4\Omega^2 R^5/h\nu^2$ and the thermal Rossby number $\mathrm{Ro_T} = g\alpha h\Delta T/\Omega^2 R^2$, where g is the gravitational acceleration, Ω is a rotation rate and ΔT is the temperature difference between the heater and the mean temperature of the upper surface. Please note, that usually the thermal Rossby number is a key parameter for the studies with a rotating cylinder gap filled with a fluid and isothermal sidewalls. Here we consider a rotating shallow cylindrical layer with non-uniform heating at the bottom and cooling at the open surface (boundary conditions of the second type) so we estimated values of $\mathrm{Ro_T}$ only for comparison with the results of other studies. The values of $\mathrm{Ro_T}$ for the regular and irregular (atmospheric) baroclinic wave regimes are presented in Table 1.

First, we examine the mean flow structure and how it changes with variations in heating power. The main and most surprising result was the robustness of the flow structure. Fig. 2a,b show the stream function fields representing the meridional circulation for the basic regime and the regime with 20% of the heating power of the basic regime. The qualitative similarity of the flow structure is evident. To see the quantitative differences, we plot the mean, mid-level profiles of the stream function for different heating power values (Fig. 2c), which show the weakening of the meridional circulation as the heating power decreases. However, the normalized profiles (Fig. 2d) practically coincide. The same result is obtained for the zonal flows (Fig. 3). The normalized profiles of zonal velocity V show only a slight variation in shape and a weak shift of the maximum zonal velocity to larger radii. A similar flow structure should result in a similar distribution of radial heat flux, which we divide into mean and pulsating parts

$$q^r_{full} = \langle U^m T^m \rangle_\phi + \langle uT' \rangle_{\phi,t},$$

where U^m,T^m are the mean (over time) radial velocity and temperature ($U^m = \langle U \rangle_t$, $T^m = \langle T \rangle_t - T_0$) and u,T' are the pulsations of radial velocity and temperature. Indeed, despite the quantitative differences, the normalized profiles of the mean and pulsating components of heat flux are nearly identical (Fig. 4). The robustness of the flow structure described here characterizes all configurations considered (two rotation rates and uniform and non-uniform

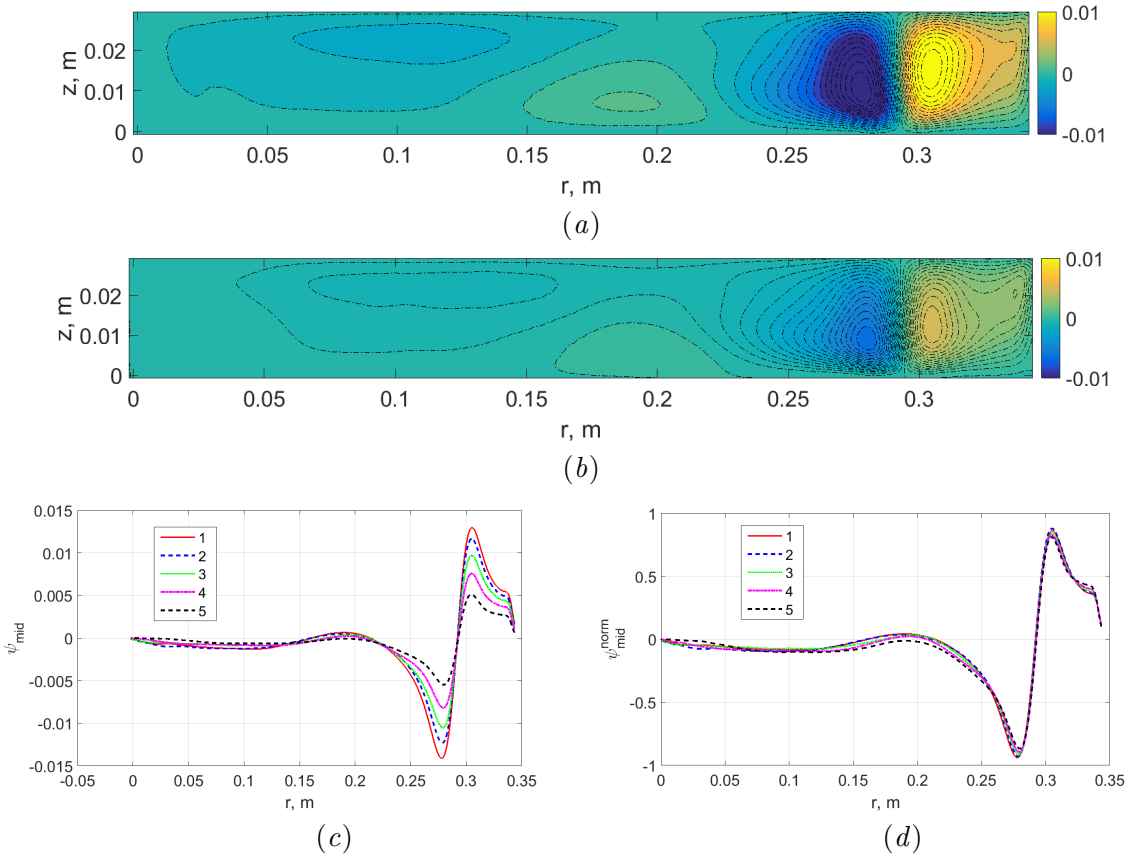

Figure 2. (a) mean meridional circulation (stream function) for the atmospheric regime, 100% heating power, (b) mean meridional circulation (stream function) for the atmospheric regime, 20% heating power, (c) mean mid-level profiles of the stream function for different values of heating power, 1 – 100%, 2 – 80%, 3 – 60%,4 – 40%, 5 – 20%, (d) the same profiles normalized to the maximum value. (Colour online)

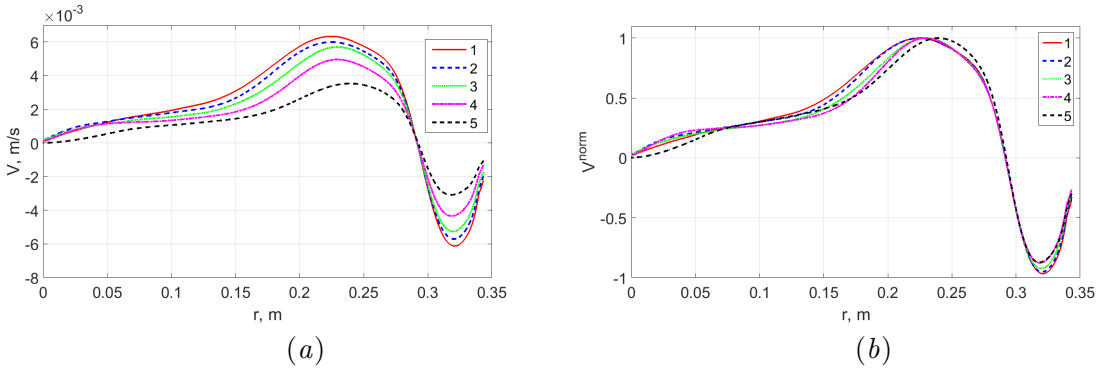

Figure 3. (a) mean top-level profiles of the zonal velocity for different values of heating power, 1 – 100%,2 – 80%, 3 – 60%,4 – 40%, 5 – 20%, (b) the same profiles normalized to the maximum value. (Colour online)

.

cooling at the upper boundary). The temperature fields are also similar (see for the typical temperature distribution Fig. 1c). The temperature profiles averaged over the layer height demonstrate that decreasing the heating power results in a gradual reduction in the radial temperature difference (Fig. 5). We note that the dependence of the mean characteristics on heating power is nonlinear (Fig. 6), and the decrease with reduced heating is significant, up to 30% of their value at full heating power.

The preservation of the mean flow structure with heating variation does not imply that the distribution and characteristics of flow fluctuations, primarily caused by baroclinic waves,

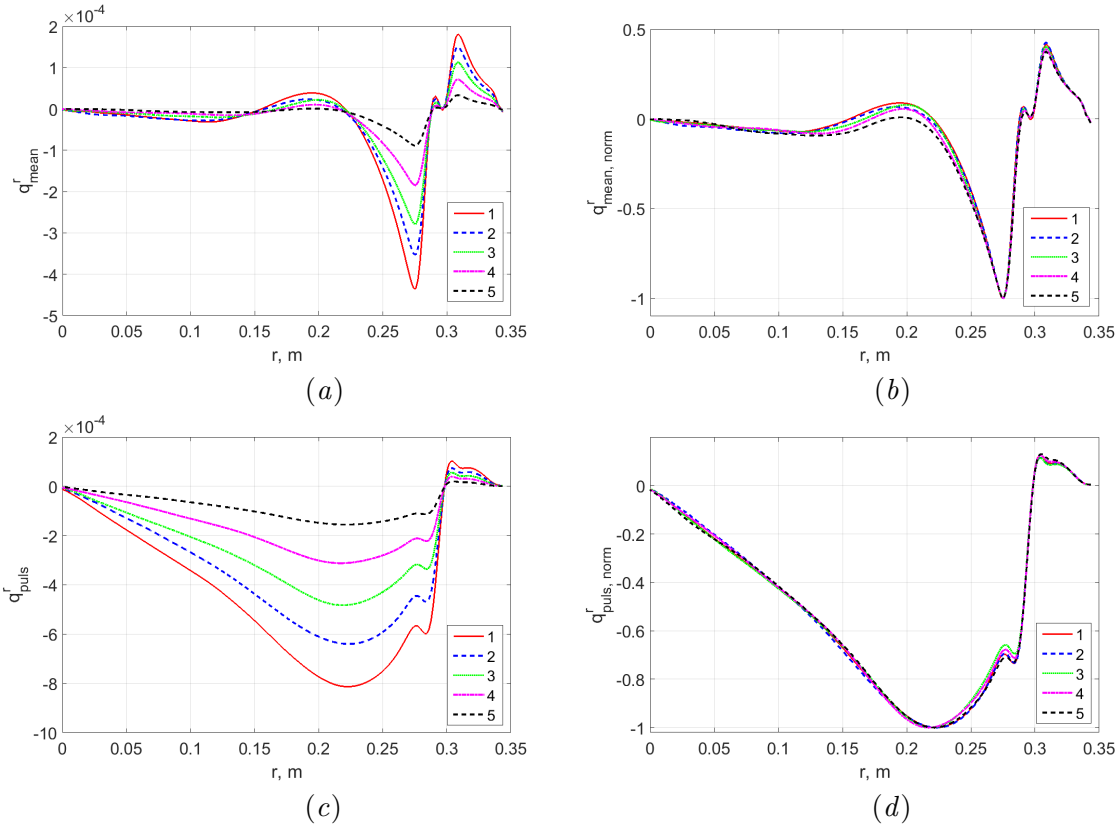

Figure 4. (a) and (c) averaged over height profiles of the mean and pulsating parts of the radial heat flux, q^r_{mean} and q^r_{puls} for different values of heating power, in K m/s; 1 – 100%, 2 – 80%, 3 – 60%, 4 – 40%, 5 – 20%, (b) and (d) the same profiles normalized to the maximum value. (Colour online)

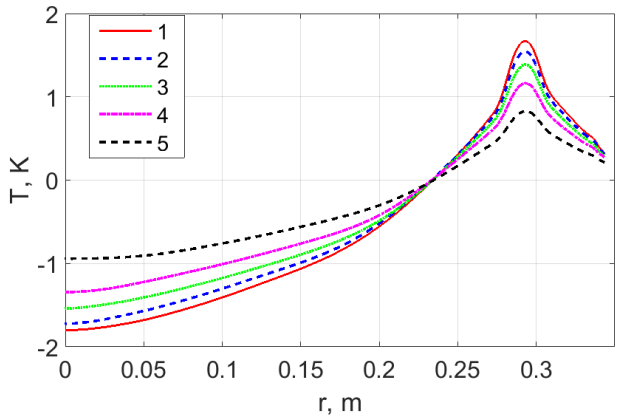

Figure 5. Mean (over height) radial temperature profiles for different values of heating power, 1 – 100%,2 – 80%, 3 – 60%,4 – 40%, 5 – 20%. (Colour online)

will be similar. Fig. 7a,b show the spatial distributions of the energy of radial velocity and temperature pulsations for the basic regime. The dimensional and normalized profiles of radial velocity pulsation energy for different heating magnitudes (Fig. 7c,d) show that they are similar as well. However, the distribution of pulsation energy only characterizes the averaged influence of the different wave modes over time. The spatial and temporal characteristics of the baroclinic waves depend strongly on the rotation rate, as can be seen clearly in the Hovmöller diagrams (Fig. 8) of the time evolution of the profiles of radial velocity pulsations. These profiles are plotted for the upper boundary and fixed radii near the maximum baroclinic wave

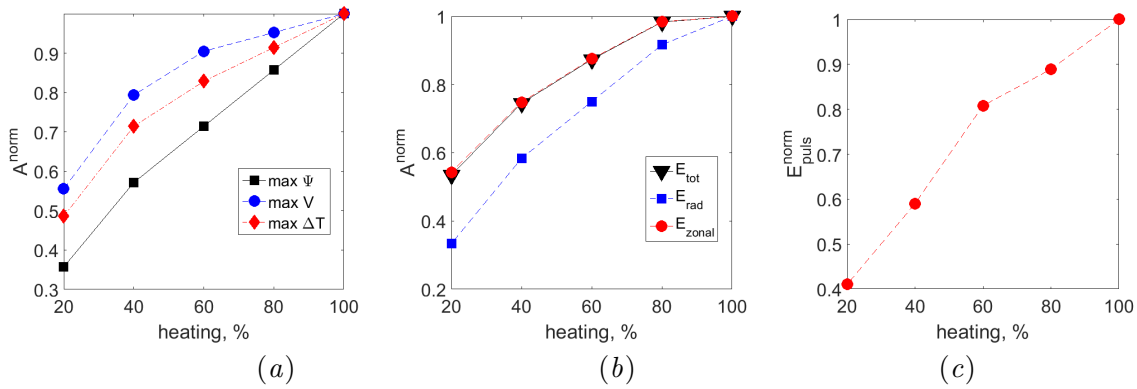

Figure 6. Dependence of the main characteristics on the heating power. (a) maximum values of stream function (at mid-level), zonal velocity and temperature difference, (b) maximum values of total energy of the mean flow, and its zonal and radial parts, (c) maximum values of energy of pulsations. All characteristics were normalized to the maximum value at 100% heating power. (Colour online)

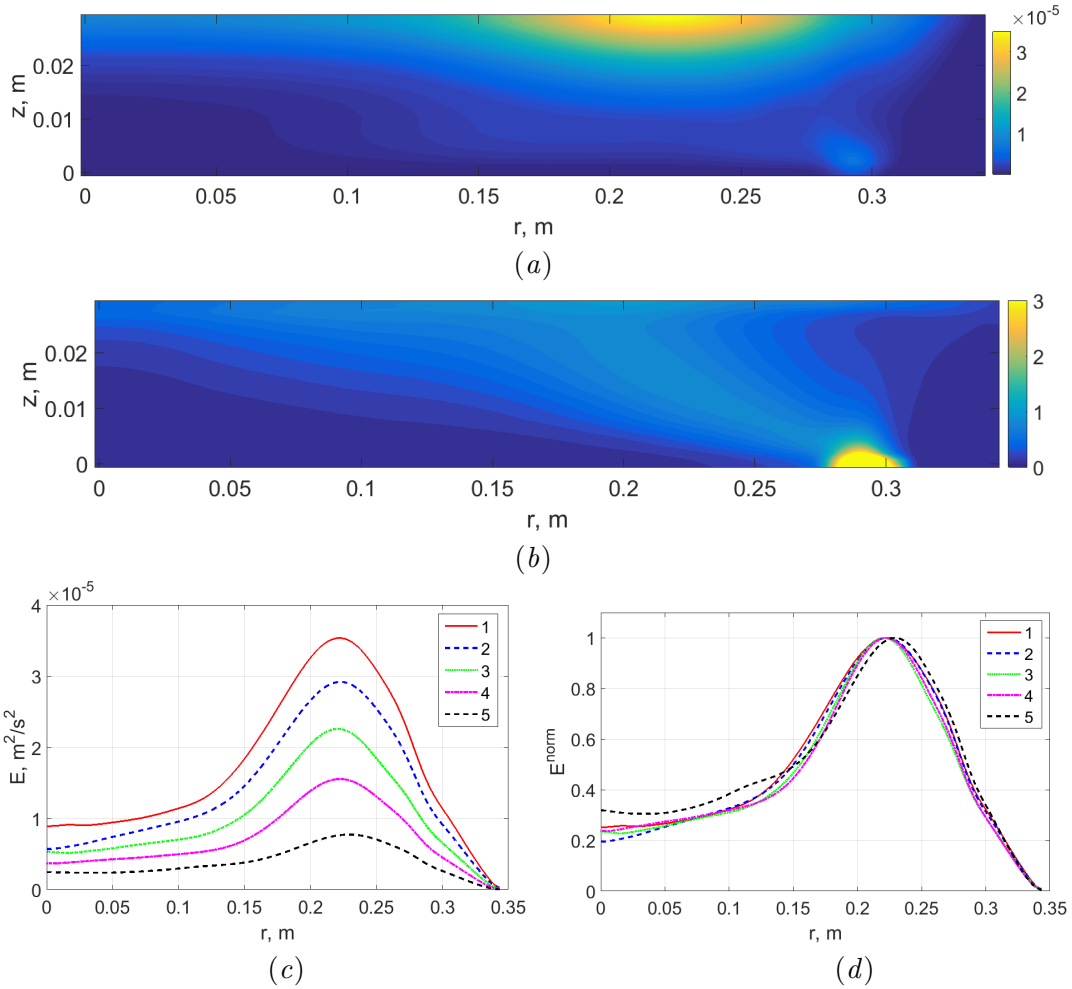

Figure 7. Mean (over time and azimuthal coordinate) distributions of energy of pulsations of radial velocity (a) and temperature (b) in a meridional cross-section, the atmospheric regime, 100% heating power, (c) mean top-level radial profiles of energy of radial velocity pulsations for different values of heating power in the atmospheric regime, 1 – 100%, 2 – 80%, 3 – 60%, 4 – 40%, 5 – 20%, (d) the same profiles normalized to the maximum value. (Colour online)

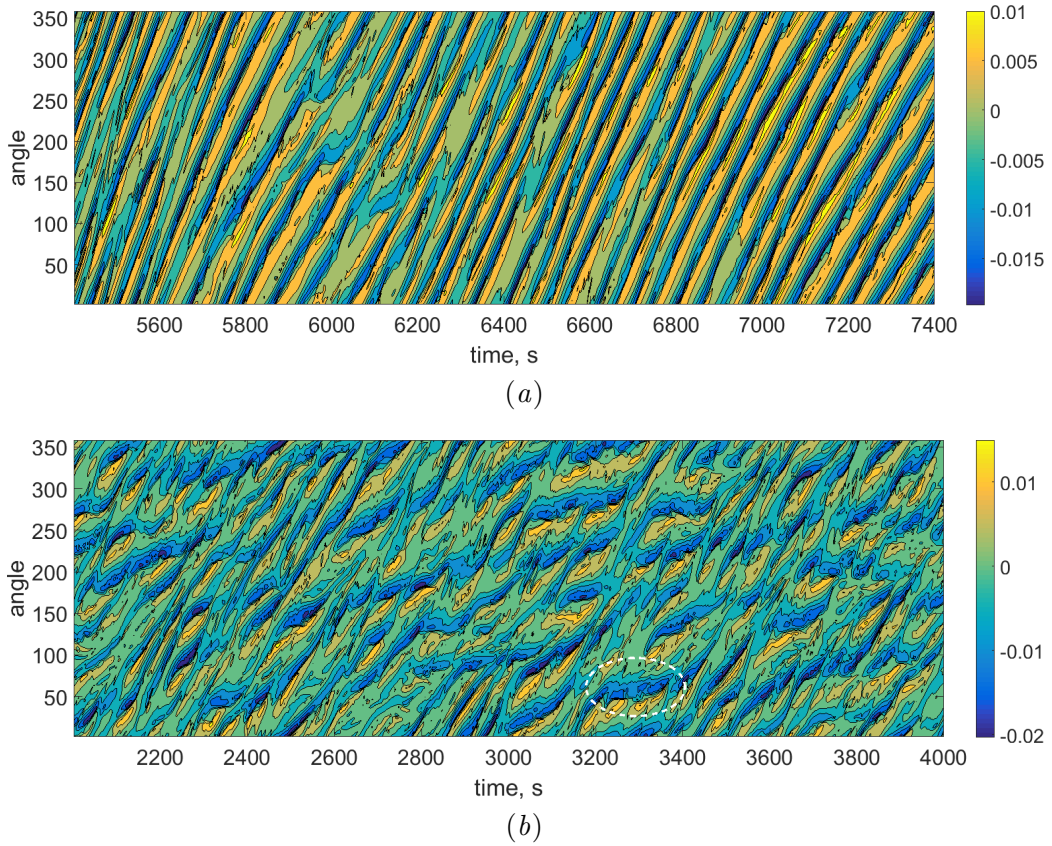

Figure 8. Hovmöller diagrams of the meridional velocity fluctuations (in m/s) for the regular wave regime (a) and atmospheric regime (b). (Colour online)

intensity ($r = 0.22$ m). These profiles are analogous to Hovmöller diagrams of meridional velocity pulsations plotted for a fixed latitude and altitude. At slower rotation rates, the baroclinic waves are more regular (Fig. 8a), though there are also transformations including variations in phase velocity (i.e., different slopes of the lines), dominant wave number, and interruptions in wave activity. The diagram for faster rotation (the atmospheric regime) is quite irregular (Fig. 8b). The elongated patterns represent the motion of individual baroclinic wave maxima, and their size indicates lifetime. Most live from five to 12 rotation periods, which is consistent with atmospheric waves. The significant variation in their slopes indicates that they move at different phase velocities. The slopes of the irregular waves are much smaller than those of the regular waves. The nearly horizontal patterns (one of which is shown by the dotted line in Fig. 8b) represent an analog of a blocking event, which occurs when a large-scale vortex remains in the same place for a sufficiently long time (more than five days). Therefore, blocking is an intrinsic feature of baroclinic waves in the irregular atmospheric regime.

To represent the vertical structure of the baroclinic waves, we plotted Hovmöller diagrams using vertical profiles of radial velocity and temperature pulsations (Fig. 9) at the same radii ($r = 0.22$ m) as before. As can be seen, the temperature pulsations are less localized vertically and horizontally than the radial velocity pulsations. The irregular atmospheric regime is characterized by a strong variation in the vertical extent of the baroclinic waves (see Fig. 9c,d). Another interesting feature of the baroclinic waves is the time lag between the temperature and radial velocity pulsations. This is clearly seen in the temporal variation of the magnitude of the pulsations, averaged over height, for the regular wave regime (Fig. 9e). In the regular regime, the time lag changes from 9 to 12 seconds as the heating power decreases. The correlation coefficient between temperature and velocity fluctuations is high (about 0.8) when the

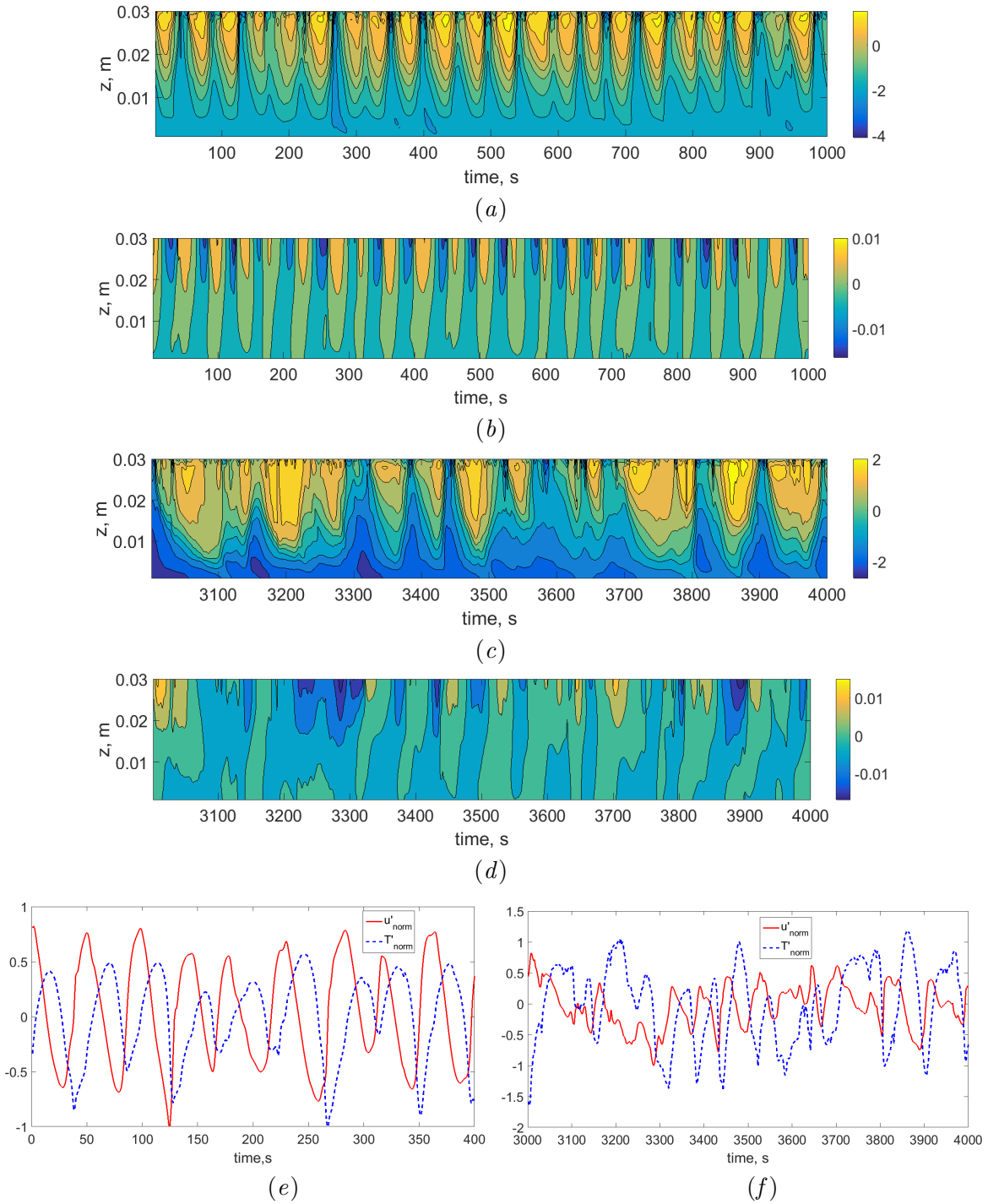

Figure 9. Hovmöller diagrams of the temperature (a,c), and meridional velocity fluctuations (b,d), for the regular wave regime (a,b) and atmospheric regime (c,d), Temperature in K, velocity in m/s. Averaged over height time, normalized by maximal values, series of radial velocity and temperature fluctuations for the regular wave regime (e) and atmospheric regime (f). (Colour online)

time lag is considered. For the irregular regime, the temperature-velocity correlation is less obvious (Fig. 9f), but the correlation coefficient is still significant, ranging from 0.5 to 0.6, with a time lag that varies similarly to that of the regular regime, from 9 to 12 seconds.

The zonal pulsations of meridional velocity at the fixed radii can be decomposed into Fourier modes, so baroclinic waves can be considered as a superposition of a number of low Fourier modes (see, for example, (Sukhanovskii *et al.* 2023, 2025)). The mean radial distributions

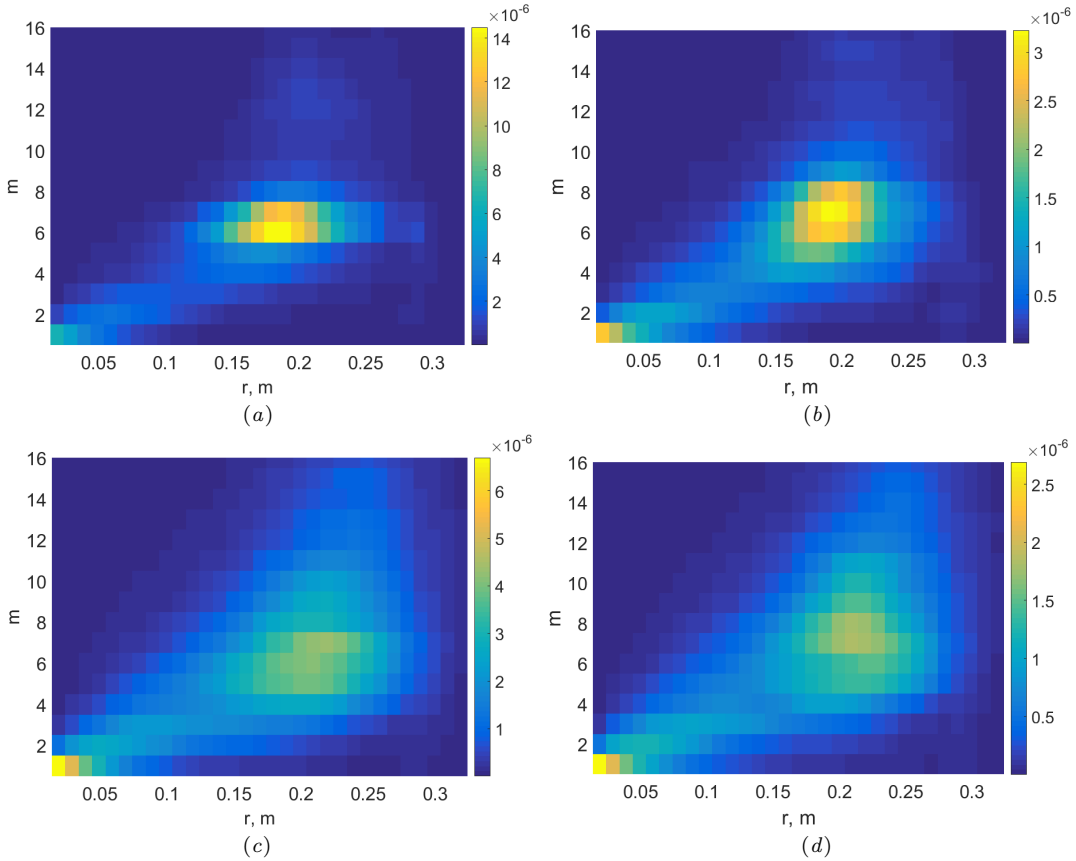

Figure 10. Mean radial distribution of the energy of main wave modes (in m^2/s^2), m – mode number; (a)-(b) regular regime, (c)-(d) atmospheric regime, (a)-(c) 100% heating power, (b)-(d) 40% heating power. (Colour online)

of the energy of the Fourier modes are presented in Fig. 10, where m is the zonal wave number. Significant differences in energy distribution exist between the regular and irregular regimes, as seen in Fig. 10a,c. Decreasing the heating power increases the number of main modes, particularly the higher modes (Fig. 10b,d). This results in a wider maximum in the m-r plane. The energy distribution in the atmospheric regime is remarkably similar to that in (Sukhanovskii *et al.* 2025), which was obtained in a zonally symmetric, full-scale, idealized simulation of an Earth-like atmosphere. The time evolution of the main modes for the two regimes is shown in Fig. 11. As seen in Fig. 11a, even the regular wave regime in a dishpan configuration is characterized by changes in the dominant wave mode and time intervals with irregular behavior. A significant decrease in heating power (up to 40% of the initial heating power) leads to noticeable destabilization of baroclinic waves (Fig. 11b). The temporal mode evolution for the atmospheric regime is irregular and similar for all heating power magnitudes considered (Fig. 11c).

The energy spectra provide full information about the energy distribution of the Fourier modes. Reduced energy spectra of the radial velocity pulsations are shown in Fig. 12a,b. For both regimes, the slopes of the spectra range between "-3" and "-4", and the spectra become steeper as heating decreases. These spectra resemble those obtained from analysis of data from over 6900 commercial aircraft flights Gage and Nastrom (1986) and in a full-scale, zonally symmetric simulation (Sukhanovskii *et al.* 2025), with slopes of "-3.5" and "-3" for the winter and summer seasons, respectively. In order to analyze local low-frequency temporal oscillations of radial velocity we calculate the continuous wavelet transform in the area of maximum baroclinic activity using the complex Morlet wavelet (see for details (Frick *et al.* 2022)). The corresponding wavelet frequency spectrum of the radial velocity pulsation

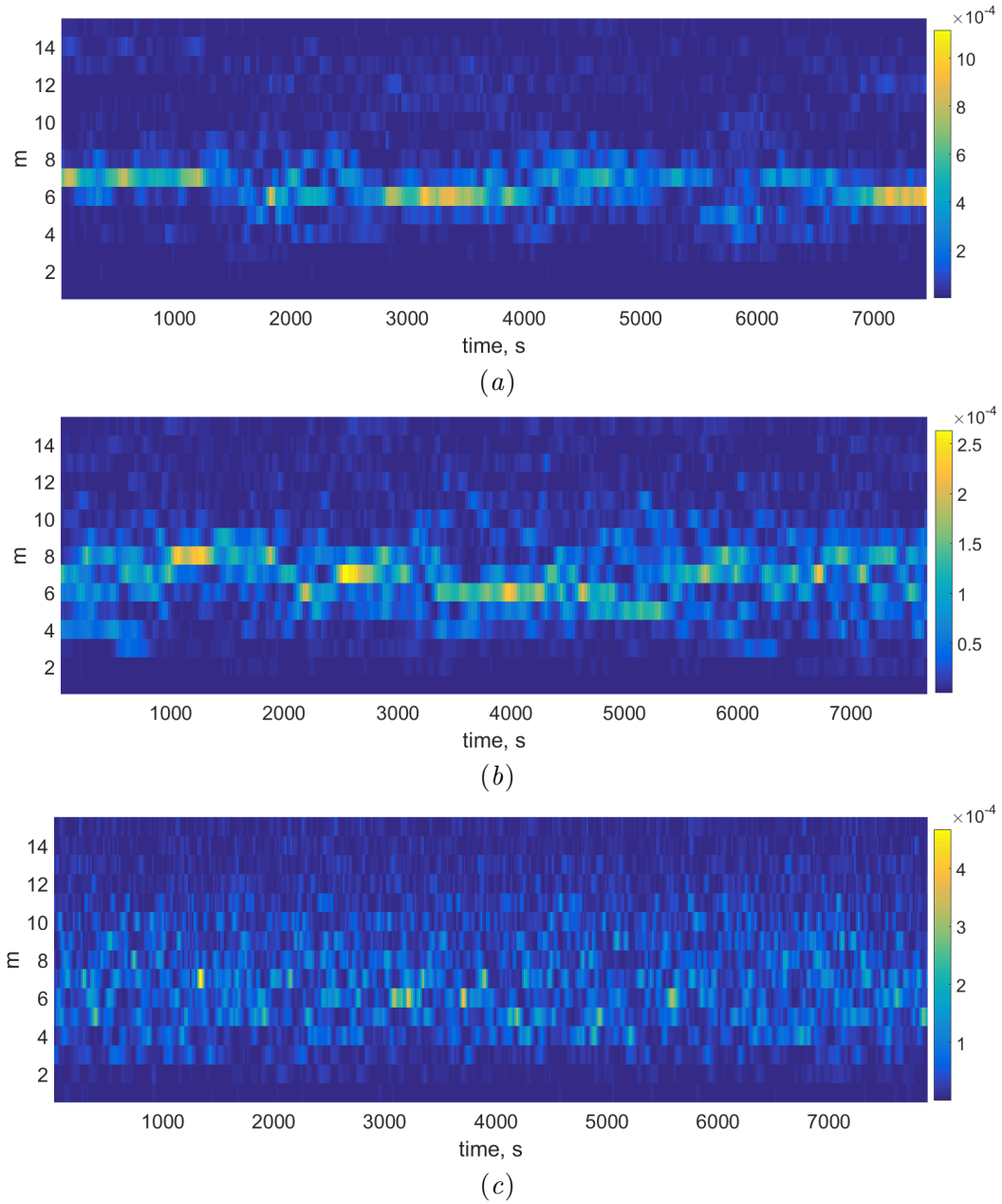

Figure 11. Temporal variation of the energy of the main modes (in m^2/s^2), (a) regular regime, 100% heating power, (b) regular regime, 40% heating power, (c) atmospheric regime, 100% heating power. (Colour online)

energy is shown in Fig. 12c. We observe that the regular regime exhibits a distinct peak due to periodic baroclinic waves. The spectra for higher frequencies are nearly identical, characterized by two intervals with slopes of "-5/3" and "-4".

The growth rate of baroclinic waves is determined by the level of baroclinicity. The Eady parameter, defined as $\Gamma = fN^{-1}\partial V/\partial z$, is a commonly used variable for estimating baroclinicity (Lindzen and Farrell 1980, Chang *et al.* 2002). Here, f is the Coriolis parameter and N is the Brunt–Väisälä frequency. In our configuration, the vertical gradient of the zonal velocity primarily determines the formation of baroclinic waves. Therefore, we used the mean vertical gradient of the zonal velocity V_{max}/h as Eady parameter in our analysis. Fig. 13 shows the normalized values of the mean vertical gradient of zonal velocity and the root mean square of radial velocity fluctuations $\mathrm{RMS}_{u'}$ (at radii of maximal baroclinic activity) for two regimes. In

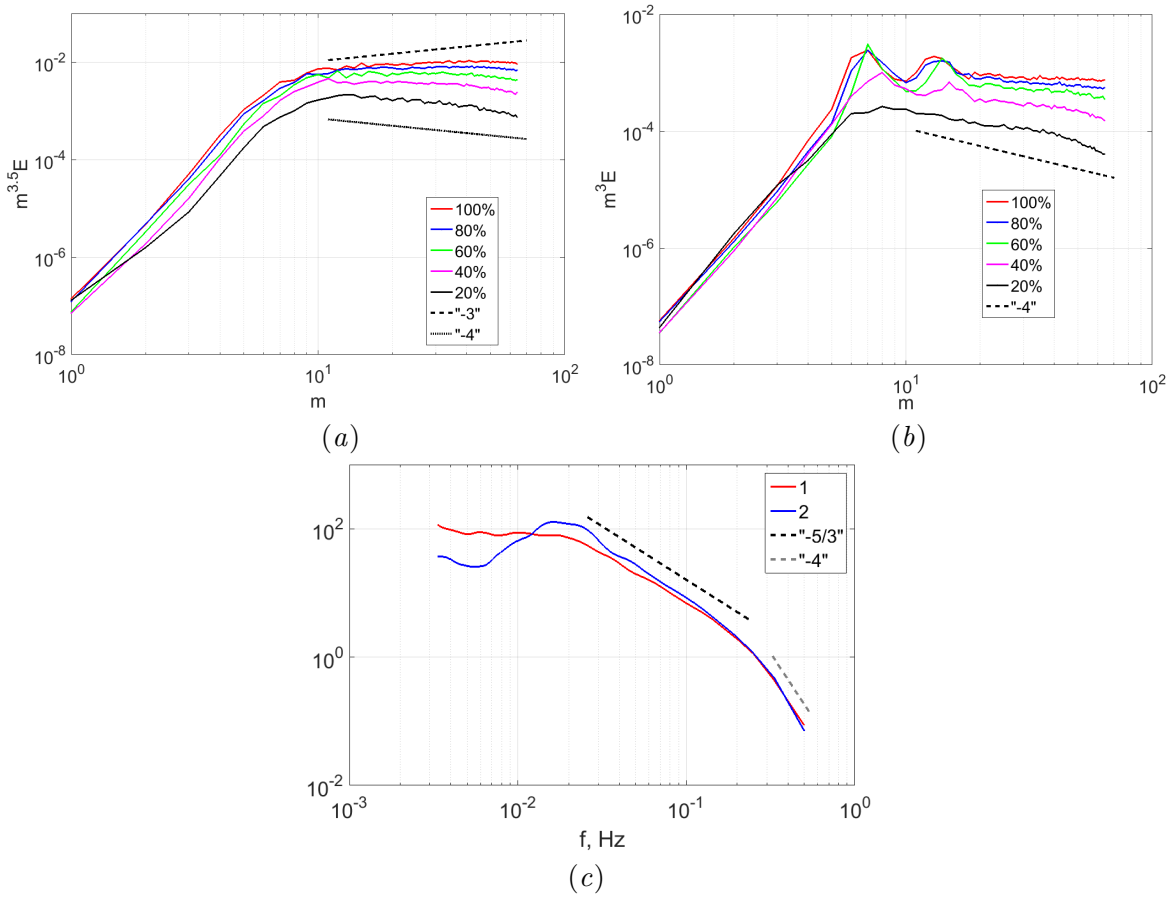

Figure 12. (a)-(b) reduced spectra of radial velocity fluctuations (energy of baroclinic waves), multiplied by $m^{3.5}$ for the atmospheric regime (a) and by m^3 for the regular wave regime (b); (c) wavelet frequency spectrum of energy of radial velocity fluctuations, 1 – atmospheric regime, 2 – regular wave regime. (Colour online)

the regular wave regime (Fig. 13a), the Eady parameter and $\mathrm{RMS}_{u'}$ change in counterphase (low-frequency part), whereas in the irregular regime (Fig. 13b), they are uncorrelated. This agrees with the assumption that the Eady parameter and baroclinic wave activity are directly related only in cases of local baroclinic wave sources in time or space (Chang *et al.* 2002). Indeed, idealized global simulations with strong seasonal variations (Sukhanovskii *et al.* 2025) showed a significant correlation between the Eady parameter and $\mathrm{RMS}_{u'}$.

Knowing the phase of each wave mode enables us to estimate its phase velocity. The phase velocities of the two main modes in the two regimes are shown in Fig. 14. To remove high-frequency noise, we use a moving average over one period of rotation. The phase velocity of the main modes in the regular regime exhibits relatively minor non-periodic fluctuations near the mean value (Fig. 14a), except during periods of low amplitude (Fig. 11a). In contrast, phase velocity fluctuations in the atmospheric regime are much more intense and frequent (Fig. 14b). The phase velocities of the main modes in both regimes are uncorrelated. Phase velocity characterizes the motion of sequences of cyclones and anticyclones embedded in zonal flows. Therefore, analyzing the dependence of the mean phase velocity of the different modes on the heating power is important (Fig. 15a,b). The phase velocity for both regimes depends on the mode number, implying dispersion of baroclinic waves in agreement with (Sukhanovskii *et al.* 2025). Additionally, except in the case of the lowest heating power value, the maximum of V_{phase} shifts towards higher modes with decreasing heating. The ratio of the maximum mean zonal velocity to the maximum mean phase velocity shows a slight dependence on heating power (Fig. 15c). This suggests that the mean phase velocity of baroclinic waves is primarily determined by the mean zonal flow velocity. This is consistent with the results obtained within

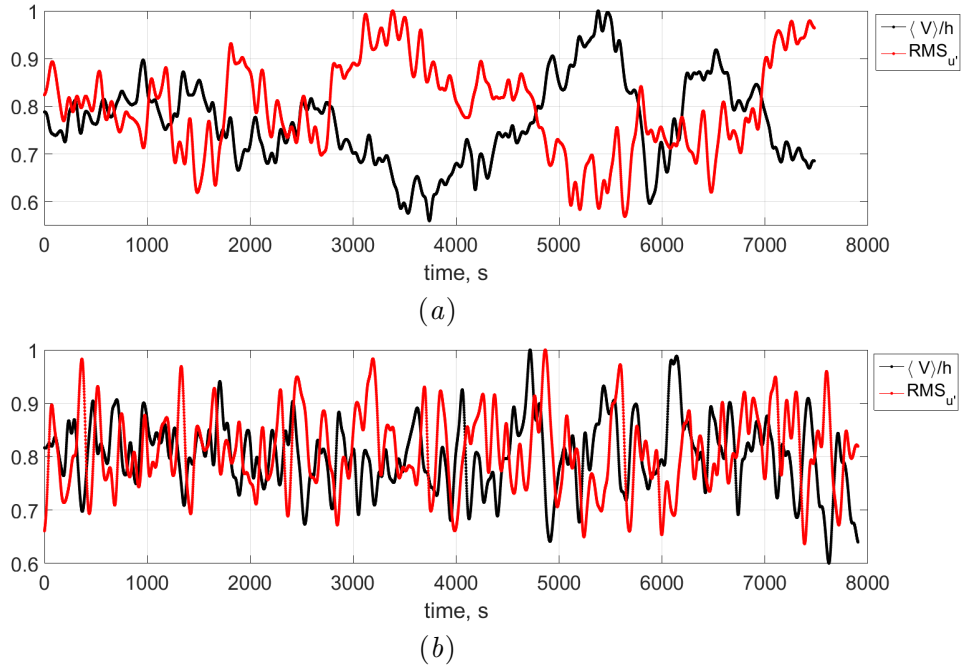

Figure 13. Temporal variation of the normalized (by maximal value) zonal velocity, and RMS fluctuations of the radial velocity, (a) regular regime, 100% heating power, (b) atmospheric regime, 100% heating power. (Colour online)

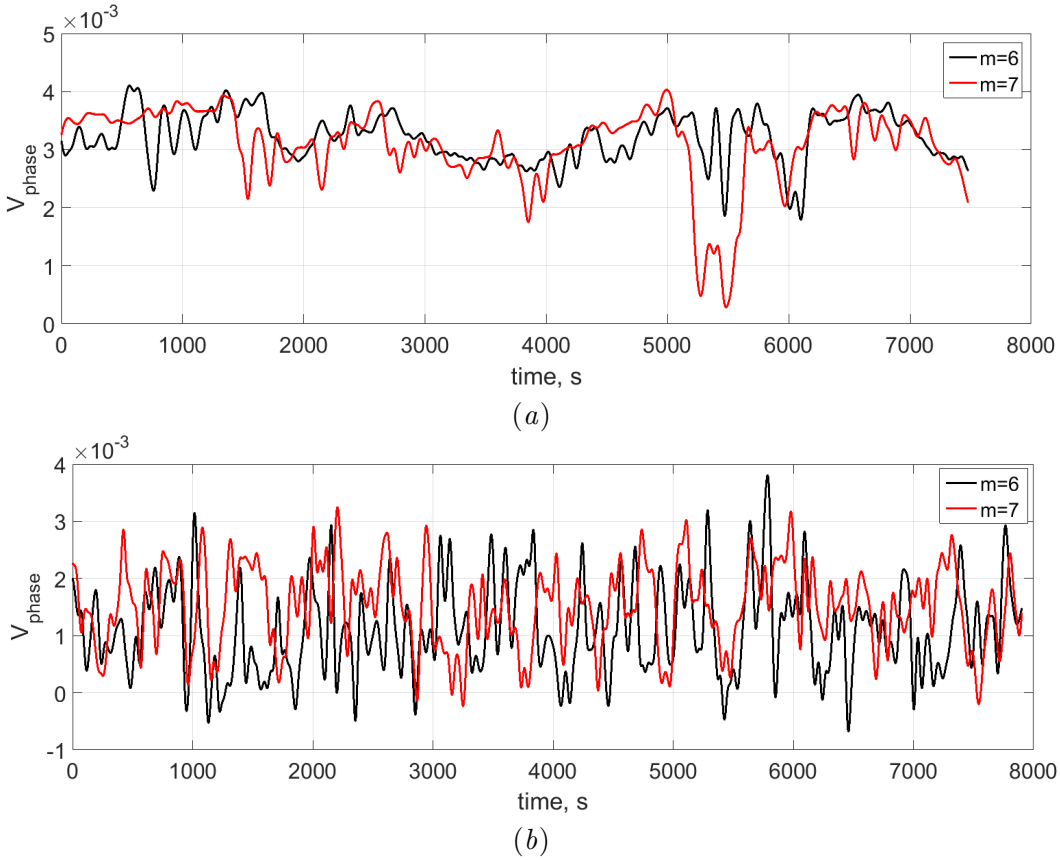

Figure 14. Temporal variation of phase velocity (in m/s) for the two main modes, (a) regular regime, 100% heating power, (b) atmospheric regime, 100% heating power. (Colour online)

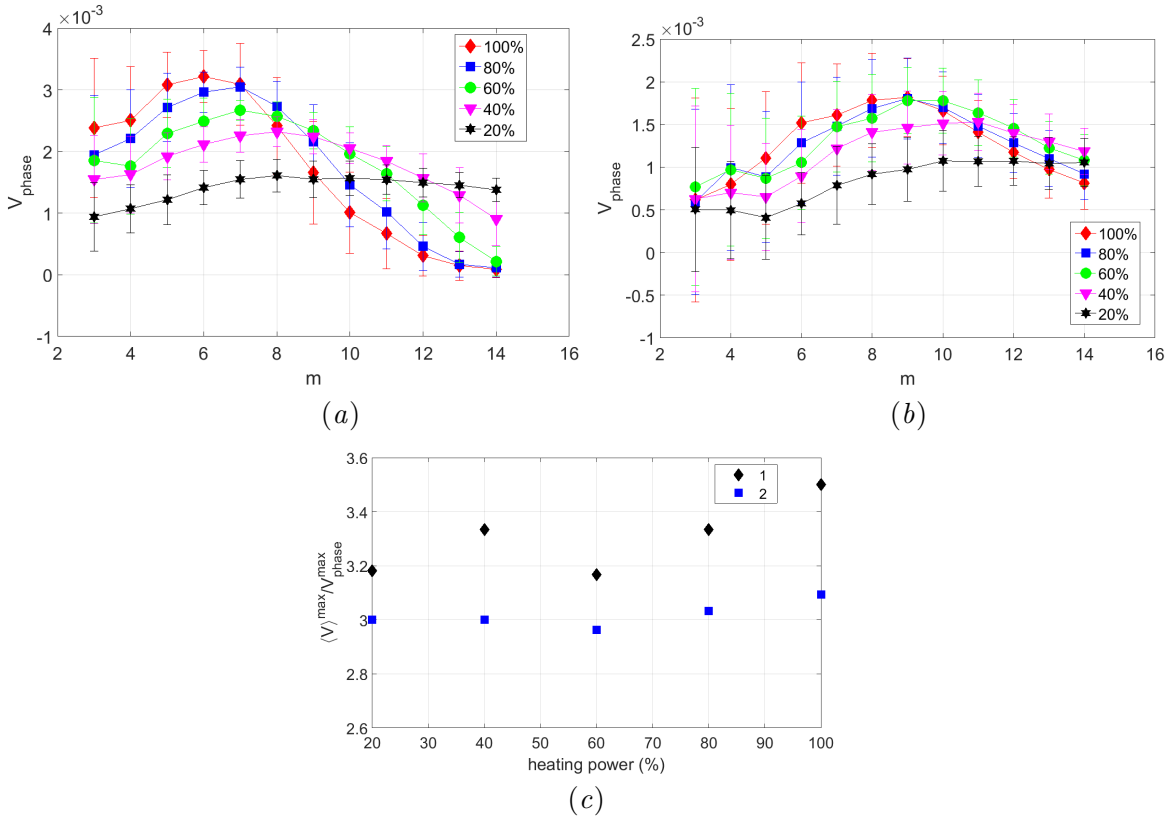

Figure 15. Mean values of the phase velocity (in m/s), (a) regular regime, 100% heating power, (b) atmospheric regime, 100% heating power, (c) ratio of the maximal mean zonal and phase velocities, 1 - atmospheric regime, 2 - regular wave regime. (Colour online)

the framework of the Eady problem (Vallis 2017).

4. Conclusion

The main objective of our research is to study how global cooling transforms the general circulation of the atmosphere. To address this question, we conducted a series of numerical simulations using a numerical analog of the laboratory model of the general atmospheric circulation. We intentionally did not consider a decrease in average temperature, i.e., we set the net heat flux to zero, as this would require significantly more computational resources. Instead, we focused on structural changes in circulation as the temperature gradient decreased. The results obtained are rather unexpected and surprising. The main result concerns the structure of the general circulation. It is very robust and practically does not change with a decrease in heating. Even at 20% of the initial heating power, the mean circulation consists of three cells: Hadley, Ferrel, and polar. However, the magnitudes of the main characteristics, such as maximum velocity and temperature difference, significantly decrease with reduced heating, reaching 30% of their values at full heating power. Therefore, the rotation rate is a key parameter that determines the structure of the global circulation (both the mean and pulsating parts), while the heating rate mainly affects the circulation's intensity and the magnitude of its main characteristics. This result is consistent with full-scale simulations of aqua-exoplanets (Kaspi and Showman 2015).

Baroclinic waves are a crucial element of mid-latitude circulation. Therefore, special attention was given to baroclinic waves and how they change with reduced heating. Even in the steady state, baroclinic waves exhibit complex temporal behavior, including variations in

phase velocity and dominant wave number, as well as interruptions in wave activity. Blocking events are observed in the atmospheric regime, meaning that blocking is an intrinsic feature of baroclinic waves in the irregular wave regime. Another interesting feature of baroclinic waves is the time lag between temperature and radial velocity pulsations. In the regular regime, the time lag increases as the heating power decreases. The correlation coefficient between temperature and velocity fluctuations is high (about 0.8) when the time lag is considered. For the irregular regime, the temperature-velocity correlation decreases; however, the correlation coefficient remains significant. These results confirm theoretical predictions that temperature and velocity shifts occur in time and space during the development of baroclinic waves.

The decomposition of baroclinic waves into Fourier modes reveals a remarkable similarity in energy distribution between the atmospheric regime and that obtained from a zonally symmetric, full-scale, idealized simulation of an Earth-like atmosphere (Sukhanovskii *et al.* 2025). It has been found that a significant decrease in the heating power results in a noticeable destabilization of baroclinic waves in both regimes under consideration. Another striking similarity was found between laboratory-scale simulations,and full-scale simulations and field observations for the energy spectra of radial pulsations. In both regimes of laboratory model, the slopes of the spectra range between "-3" and "-4" and the steepness increases as the heating decreases. It leads to the conclusion that the distribution of energy of pulsations and the transfer of energy over scales in the baroclinic wave regime are specific and can be reproduced by models with different degrees of idealization.

The Eady parameter is often used to describe the intensity of the wave activity. In our simulations in the atmospheric regime with zonally symmetric, fixed boundary conditions, the Eady parameter and the RMS of radial velocity fluctuations were not correlated. It agrees with the assumption that Eady parameter and baroclinic wave activity are directly related only in the case of local in time or space baroclinic wave sources (Chang *et al.* 2002).

The mean phase velocity of baroclinic waves is primarily determined by the mean zonal flow velocity, which is consistent with the results obtained within the framework of the Eady problem (Vallis 2017).

The results of the numerical simulation of the laboratory model of general atmospheric circulation under global cooling cannot be directly extrapolated to the real atmosphere. However, the good agreement between the laboratory- and full-scale modeling results suggests that fundamental properties of the general atmospheric circulation depend mainly on the rotation rate and meridional heating. The main outcome of our idealized simulations is the robustness of the general atmospheric circulation, which survives even a significant decrease in heating. According to our results, neither volcanic nor nuclear winter will lead to significant changes in atmospheric circulation or related variations in regional climate. The main catastrophic consequences will be related to the inevitable decrease in average temperature.

Authors' contributions Both authors contributed equally.

Funding The study was done under the RSF project 22-61-00098.

Data availability The data acquired during this study are available from the corresponding author upon reasonable request.

Declarations

Conflict of interest The authors declare no competing interests.

Ethical approval Not applicable.

References

Batalov, V., Sukhanovsky, A. and Frick, P., Laboratory study of differential rotation in a convective rotating layer. *Geophysical and Astrophysical Fluid Dynamics*, 2010, **104**, 349–368.

Blackport, R. and Screen, J.A., Insignificant effect of Arctic amplification on the amplitude of midlatitude atmospheric waves. *Science advances*, 2020, **6**, eaay2880.

Chang, E.K., Lee, S. and Swanson, K.L., Storm track dynamics. *Journal of climate*, 2002, **15**, 2163–2183.

Coupe, J. and Robock, A., The influence of stratospheric soot and sulfate aerosols on the Northern Hemisphere wintertime atmospheric circulation. *Journal of Geophysical Research: Atmospheres*, 2021, **126**, e2020JD034513.

DallaSanta, K., Gerber, E.P. and Toohey, M., The circulation response to volcanic eruptions: The key roles of stratospheric warming and eddy interactions. *Journal of Climate*, 2019, **32**, 1101–1120.

Frick, P.G., Sokoloff, D.D. and Stepanov, R.A., Wavelets for the space-time structure analysis of physical fields. *Physics Uspekhi*, 2022, **65**, 62–89.

Fultz, D., Long, R.R., Owens, G.V., Bohan, W., Kaylor, R. and Weil, J., *Studies of thermal convection in a rotating cylinder with some implications for large-scale atmospheric motions*, 1959 (Boston: American Meteorological Society).

Gage, K.S. and Nastrom, G.D., Theoretical interpretation of atmospheric wavenumber spectra of wind and temperature observed by commercial aircraft during GASP. *Journal of Atmospheric Sciences*, 1986, **43**, 729–740.

Gavrilov, A., Sukhanovskii, A., Vasiliev, A. and Popova, E., Numerical study of structural changes in the laboratory model of the atmospheric general circulation under variation of the rotation rate. *International Journal of Heat and Mass Transfer*, 2025, **241**, 126676.

Harlander, U., Kurgansky, M.V., Speer, K. and Vincze, M., Baroclinic instability from an experimental perspective. *Comptes Rendus. Physique*, 2024, **25**, 1–48.

Harlander, U., Sukhanovskii, A., Abide, S., Borcia, I.D., Popova, E., Rodda, C., Vasiliev, A. and Vincze, M., New Laboratory Experiments to Study the Large-Scale Circulation and Climate Dynamics. *Atmosphere*, 2023, **14**, 836.

Hide, R., Some experiments on thermal convection in a rotating liquid. *Q. J. Roy. Meteor. Soc.*, 1953, **79**, 161–161.

Kaspi, Y. and Showman, A.P., Atmospheric dynamics of terrestrial exoplanets over a wide range of orbital and atmospheric parameters. *The Astrophysical Journal*, 2015, **804**, 60.

Lindzen, R. and Farrell, B., A simple approximate result for the maximum growth rate of baroclinic instabilities. *Journal of the Atmospheric Sciences*, 1980, **37**, 1648–1654.

Marshall, L.R., Maters, E.C., Schmidt, A., Timmreck, C., Robock, A. and Toohey, M., Volcanic effects on climate: recent advances and future avenues. *Bulletin of Volcanology*, 2022, **84**, 54.

Meletti, G., Abide, S., Harlander, U., Raspo, I. and Viazzo, S., On the influence of the heat transfer at the free surface of a thermally driven rotating annulus. *Physics of Fluids*, 2025, **37**, 034101.

Read, P.L., Pérez, E.P., Moroz, I.M. and Young, R.M., General circulation of planetary atmospheres: insights from rotating annulus and related experiments. *Modeling Atmospheric and Oceanic Flows: Insights from Laboratory Experiments and Numerical Simulations*, 2014, pp. 7–44.

Rodda, C., Harlander, U. and Vincze, M., Jet stream variability in a polar warming scenario–a laboratory perspective. *Weather and Climate Dynamics*, 2022, **3**, 937–950.

Schneider, T., The general circulation of the atmosphere. *Annu. Rev. Earth Planet. Sci.*, 2006, **34**, 655–688.

Smith, D.M., Screen, J.A., Deser, C., Cohen, J., Fyfe, J.C., García-Serrano, J., Jung, T., Kattsov, V., Matei, D., Msadek, R. *et al.*, The Polar Amplification Model Intercomparison Project (PAMIP) contribution to CMIP6: investigating the causes and consequences of polar amplification. *Geoscientific Model Development*, 2019, **12**, 1139–1164.

Sukhanovskii, A., Gavrilov, A., Popova, E. and Vasiliev, A., The study of the impact of polar warming on global atmospheric circulation and mid-latitude baroclinic waves using a laboratory analog. *Weather and Climate Dynamics*, 2024, **5**, 863–880.

Sukhanovskii, A., Popova, E. and Vasiliev, A., A shallow layer laboratory model of large-scale atmospheric circulation. *Geophysical & Astrophysical Fluid Dynamics*, 2023, pp. 1–22.

Sukhanovskii, A., Stepanov, R., Bykov, A., Vetrov, A., Kalinin, N. and Frick, P., Mid-latitude baroclinic waves in a zonally homogeneous Earth-like planet. *Climate Dynamics*, 2025, **63**, 1–21.

Tian, W., Huang, J., Zhang, J., Xie, F., Wang, W. and Peng, Y., Processes in Climate Change: Advances and Challenges. *Adv. Atmos. Sci.*, 2023, **40**, 1379–1400.

Timmreck, C., Modeling the climatic effects of large explosive volcanic eruptions. *Wiley Interdisciplinary Reviews: Climate Change*, 2012, **3**, 545–564.

Vallis, G.K., *Atmospheric and oceanic fluid dynamics*, 2017 (Cambridge: Cambridge University Press).

Vasiliev, A., Popova, E. and Sukhanovskii, A., The flow structure in a laboratory model of general atmosphere circulation. *Computational Continuum Mechanics*, 2023, **16**, 321–331.

Vincze, M., Borcia, I.D. and Harlander, U., Temperature fluctuations in a changing climate: an ensemble-based experimental approach. *Scientific reports*, 2017, **7**, 254.

Ye, K., Woollings, T., Sparrow, S.N., Watson, P.A. and Screen, J.A., Response of winter climate and extreme weather to projected Arctic sea-ice loss in very large-ensemble climate model simulations. *npj Climate and*

Atmospheric Science, 2024, **7**, 20.

You, Q., Cai, Z., Pepin, N., Chen, D., Ahrens, B., Jiang, Z., Wu, F., Kang, S., Zhang, R., Wu, T. *et al.*, Warming amplification over the Arctic Pole and Third Pole: Trends, mechanisms and consequences. *Earth-Science Reviews*, 2021, **217**, 103625.

Zhou, S. and Liu, F., Southern Hemisphere Volcanism Triggered Multi-year La Niñas during the Last Millennium. *Adv. Atmos. Sci.*, 2024, **42**, 587–592.

Zuo, M., Zhou, T., Man, W., Chen, X., Liu, J., Liu, F. and Gao, C., Volcanoes and Climate: Sizing up the Impact of the Recent Hunga Tonga-Hunga Ha'apai Volcanic Eruption from a Historical Perspectivee. *Adv. Atmos. Sci.*, 2022, **39**, 1986–1993.